ACS Photonics

Open Access

This article is licensed under CC-BY-NC-ND 4.0

pubs.acs.org/journal/apchd5

Article

Visible-Telecom Entangled-Photon Pair Generation with Integrated Photonics: Guidelines and a Materials Comparison

Published as part of ACS Photonics special issue "Rising Stars in Photonics".

Liao Duan, Trevor J. Steiner, Paolo Pintus, Lillian Thiel, Joshua E. Castro, John E. Bowers, and Galan Moody*

Cite This: *ACS Photonics* 2025, 12, 118–127

Read Online

ACCESS | Metrics & More | Article Recommendations | Supporting Information

ABSTRACT: Correlated photon-pair sources are key components for quantum computing, networking, synchronization, and sensing applications. Integrated photonics has enabled chip-scale sources using nonlinear processes, producing high-rate time−energy and polarization entanglement at telecom wavelengths with sub-100 microwatt pump power. Many quantum systems operate in the visible or near-infrared ranges, necessitating visible-telecom entangled-pair sources for connecting remote systems via entanglement swapping and teleportation. This study evaluates biphoton pair generation and time−energy entanglement through spontaneous four-wave mixing in various nonlinear integrated photonic materials, including silicon nitride, lithium niobate, aluminum gallium arsenide, indium gallium phosphide, and gallium nitride. We demonstrate how geometric dispersion engineering facilitates phase-matching for each platform and reveals unexpected results, such as robust designs to fabrication variations and a Type-1 cross-polarized phase-matching condition for III−V materials that expands the operational wavelength range.

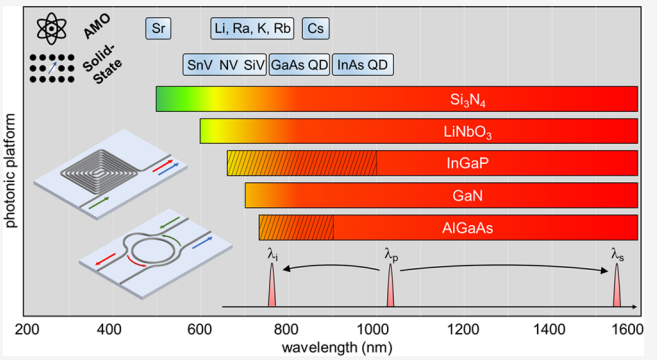

KEYWORDS: *Entanglement, photon pairs, nonlinear photonics, integrated photonics, microring resonators, four-wave mixing*

Downloaded via 95.90.255.227 on February 26, 2025 at 06:28:19 (UTC).
See https://pubs.acs.org/sharingguidelines for options on how to legitimately share published articles.

INTRODUCTION

Large-scale quantum networks and communication systems require a diverse set of components for generating, processing, storing, and transmitting quantum information with low loss and high fidelity.[1,2] For fiber-based networks, these requirements present unique challenges, as many quantum platforms that are being developed for quantum memories, repeaters, and processors, including color centers in solids,[3] trapped ions,[4,5] neutral atoms,[6,7] and semiconductor quantum dots,[8,9] operate in the visible and near-infrared wavelength range (Figure 1). Interconnecting such platforms in a quantum network may be possible through the coherent conversion of emitted photons to telecom wavelengths, but quantum frequency conversion introduces new challenges in designing appropriate systems for specific wavelengths and filtering the strong optical pump required for efficient photon number conversion.[10−13] An alternative approach to bridge the visible-telecom wavelength gap is through broadband entanglement generation with suitably designed and engineered nonlinear optical platforms.[14] In this scheme, remote quantum nodes can be entangled through successive entanglement swapping operations via a Bell-state measurement at a central node.

Quantum information can be encoded using several different degrees of freedom of photons,[15] including spatial path,[16] frequency-bin,[17] time-bin,[18] polarization,[19] and transverse mode.[20] In bulk nonlinear crystals and optical fibers, polarization-entangled pairs can be generated through spontaneous parametric down conversion (SPDC), a $\chi^{(2)}$ process in which one pump photon is annihilated to create signal and idler photons at twice the pump wavelength. Bulk optical systems, such as nonlinear crystals that are double-side pumped in a Sagnac interferometer, can generate > 10^8 polarization-entangled pairs per second with 10s to 100s of milliwatts of pump power, which has been leveraged for terrestrial and space-based quantum communications.[21,22] The techniques of polarization entanglement have been translated to integrated photonic waveguides fabricated with $\chi^{(2)}$ materials such as AlGaAs and $LiNbO_3$,[23−25] which is driven

Received: July 5, 2024
Revised: November 4, 2024
Accepted: November 5, 2024
Published: November 25, 2024

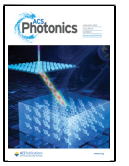

© 2024 The Authors. Published by American Chemical Society

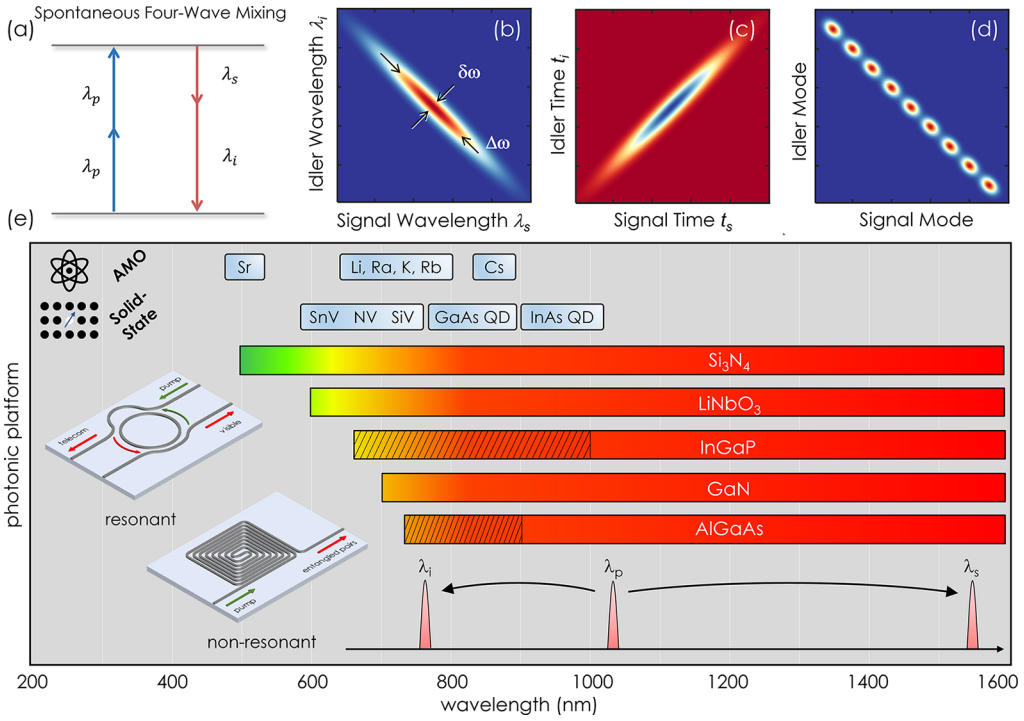

Figure 1. (a) Quantum light generation with integrated photonics utilizing spontaneous four-wave mixing in which two pump photons (λ_p) are converted into correlated signal (λ_s) and idler (λ_i) photon pairs. (b,c) Illustrative joint spectral and temporal intensities are shown for photon-pairs exhibiting a high degree of time−energy entanglement. The width along the diagonal is determined by the pump bandwidth $\delta\omega$, while the length along the antidiagonal is given by the lesser of the phase-matching function ϕ_{pm}, the transmission window T, or the spectral bandwidth $\Delta\omega$. (d) Discrete joint spectral intensity for resonant sources. (e) Comparison of the wavelength ranges for entangled photon pair generation across different material platforms. Entangled pairs can be generated at any two wavelengths within the range specified by the bar via waveguide geometry tailoring to achieve phase matching. For AlGaAs and InGaP, the shaded area indicates the extended wavelength range enabled by employing cross-polarized spontaneous four-wave mixing.

by the need for compact and power-efficient quantum light sources in quantum information applications.[2]

While integrated polarization-based devices require careful mode engineering to ensure high fidelity entanglement,[26] integrated photonics using a single polarization mode can also generate time−energy correlated pairs—another form of entanglement that is finding immediate applications in quantum key distribution[27] and quantum computing.[28] Time−energy correlated pairs can be created through spontaneous four-wave mixing (SFWM) in waveguides, whereby two pump photons are annihilated to generate a signal-idler pair simultaneously but probabilistically within the coherence time of the pump, as illustrated by the energy diagram and joint spectral and temporal intensities in Figure 1(a−d). Through modal and pump spectral engineering, these correlations can create a biphoton time−energy entangled state as originally pointed out by Franson.[29] The biphoton state can be described by

$$|\psi\rangle \propto \iint \Theta(\lambda_s, \lambda_i)\Psi(\lambda_s, \lambda_i)\mathrm{d}\lambda_s\, \mathrm{d}\lambda_i |1\rangle_s |1\rangle_i \tag{1}$$

where Θ is the spectral envelope of the pump and $\Psi(\lambda_s, \lambda_i) = \phi_{pm}(\lambda_s, \lambda_i)T(\lambda_s)T(\lambda_i)$ is determined by the phase-matching function (ϕ_{pm}) and the amplitude transmission function (T). Conventionally, $\phi_{pm} = \mathrm{sinc}(\Delta kL)$, where $\Delta k = 2k_p - k_s - k_i$ is the linear phase matching function in terms of wavenumbers k and L is the propagation length. The joint spectral intensity (JSI) is determined from the magnitude squared of the joint spectral amplitude $\Theta(\lambda_s,\lambda_i) \times \Psi(\lambda_s,\lambda_i)$. In any device configuration, the shape of the JSI function is governed by energy conservation and phase-matching and is widely used to characterize and distinguish between different biphoton states to quantify the degree of time−energy entanglement through Schmidt decomposition.[30] With large spectral correlations ($\delta\omega \ll \Delta\omega$), the biphoton wave function is not separable, and such time−energy entangled pairs have been utilized to create time-bin or frequency-bin qubits using Franson interferometers or frequency modulation and shaping, respectively.[15,31] In the case of weak spectral correlations ($\delta\omega \approx \Delta\omega$), the separable biphoton wave function has been utilized for path-encoded qubits for chip-scale quantum computing and heralded single-photon generation.[16,32]

Resonant and nonresonant integrated photonic devices have been developed in several material platforms for photon-pair generation primarily in the telecom C-band, with less research devoted to the generation of signal-idler pairs in different spectral windows, such as visible-telecom. Several approaches to visible-telecom biphoton pair generation have been pursued, including nonlinear optical fibers,[33] periodically poled bulk nonlinear crystals,[34] and integrated photonic microresonators.[35] In bulk crystals and fibers, polarization-entangled pairs can be generated over a broad continuous spectral band. Spectral filtering is required to carve out signal-idler pairs, which reduces the useful pair generation rate and efficiency for applications such as entanglement swapping. In the approach with integrated photonic resonators, the incorporation of the nonlinear medium within the cavity enhances the entangled-pair generation efficiency. Using a stoichiometric Si_3N_4 microresonator, for example, Lu et al. generated visible-

https://doi.org/10.1021/acsphotonics.4c01238
ACS Photonics 2025, 12, 118−127

telecom time−energy entangled-photon pairs between 668 and 1548 nm with high photon-pair generation rate (PGR), coincidence-to-accidental ratio (CAR), and two-photon visibility with submilliwatt optical pump power.[14] The wide bandgap of Si_3N_4 makes it appealing for broadband pair generation; however, it also has a weak $\chi^{(3)}$ optical nonlinearity compared with other nonlinear integrated photonic materials.[15]

To this end, we examine different leading integrated photonic materials capable of visible-telecom time−energy entangled-photon pair generation including silicon nitride (SiN), lithium niobate (LN), aluminum gallium arsenide (AlGaAs), indium gallium phosphide (InGaP), and gallium nitride (GaN). Using known dispersion curves for each material, we examine the optimal designs for phase-matched spontaneous four-wave mixing across the widest bandwidth spanning 1550 nm to the visible spectrum, covering several leading quantum memory and optical clock platforms such as quantum emitters in diamond and hexagon boron nitride (hBN), III−V quantum dots (QDs), and atomic systems including strontium (Sr), lithium (Li), radium (Ra), potassium (K), and rubidium (Rb). We then compare the performance of each platform in terms of the entangled-pair brightness and bandwidth. We find that, of the materials examined, SiN provides the broadest wavelength separation of the signal-idler entangled photons due to its wide bandgap and flat dispersion, whereas III−V materials such as InGaP and AlGaAs offer the highest pair generation rates. Importantly, we find a novel Type-1 cross-polarized phase-matching scheme for InGaP and AlGaAs, extending the idler photon further into the visible regime as indicated by the shaded regions in Figure 1. By analyzing the phase-matching conditions, we find optimal designs that simultaneously maximize the pair-generation rates and are highly tolerant of fabrication process variations, making these designs robust, scalable, and efficient for entanglement distribution.

METHODS

Material Properties. When designing and configuring integrated photonic broadband entangled-photon pair sources, different semiconductor materials offer different advantages. Platforms like SiN are compatible with foundry manufacturing, facilitating the use of process design kits, mature fabrication and processing, and a wide bandgap that extends the accessible wavelength range for photon-pair generation. Additionally, SiN, known for its moderate third-order nonlinearity, can also achieve low-loss waveguides that can enhance the generation efficiency and allow for low-loss passive components to be created on the chip. Materials such as AlGaAs, InGaP, and GaN excel in pair generation efficiency through SFWM due to large third-order nonlinear coefficients and high refractive index contrast, but these platforms are not yet scalable at foundry levels and were historically limited by high propagation losses. Recent advancements have significantly reduced these losses to levels comparable to state-of-the-art silicon waveguides at telecom wavelengths around 1550 nm, making these platforms the brightest for pair generation at 1550 nm via SFWM and SPDC.[36−39]

Entangled photon pairs are typically produced through nonlinear optical processes: SPDC in $\chi^{(2)}$ materials and SFWM in $\chi^{(3)}$ materials, both adhering to energy conservation laws with $\omega_p = \omega_s + \omega_i$ for SPDC and $2\omega_p = \omega_s + \omega_i$ for SFWM.[40,41] For pair generation across visible and telecom wavelengths, SFWM is preferred because it uses more accessible pump wavelengths near 1,000 nm, unlike the 300−700 nm required for SPDC-based sources.

In addition to energy conservation that specifies the frequency of generated photons, the momentum should also be conserved. This condition is described by the wavevector mismatch formula

$$\Delta k = k_i + k_s - 2k_p \tag{2}$$

where $k = 2\pi n_{eff}/\lambda$, n_{eff} is the effective refractive index, and $\Delta k = 0$ ensures momentum conservation. Achieving the phase-matching condition is challenging due to material and waveguide dispersion, which cause the effective index to vary with wavelength. Rewriting this condition in terms of angular frequency and effective index gives an expression for the frequency mismatch

$$\omega_s n_s + \omega_i n_i = 2\omega_p n_p \tag{3}$$

where n_s, n_i, and n_p are the values of the effective indices at angular frequencies ω_s, ω_i, and ω_p, respectively. Here, we only consider linear contributions, i.e., we ignore nonlinear effects such as self-phase modulation and cross-phase modulation, which we find have negligible impact on the designs in this study for both straight waveguides and ring resonators (see Supporting Information).

As a representative demonstration, we model different material platforms by pumping at 1033.3 nm and generating the entangled pairs at 1550 and 775 nm, motivated in part by near-IR transitions of the hyperfine levels of potassium and rubidium.[42] Different wavelengths can also be chosen to connect different systems. To achieve zero phase mismatch, following eq 3, we must satisfy the following equation: $2n_s + n_i = 3n_p$. Two routes are possible: search for a material system and geometry that yields identical values for n_i, n_s, and n_p, or manipulate the waveguide geometry for a given material system to achieve a quasi-linear dependence on the effective index such that the increase in effective index of the idler mode is offset by a corresponding reduction in the effective index of the signal mode. Intuitively, from Figure 2, GaN, SiN, and LN

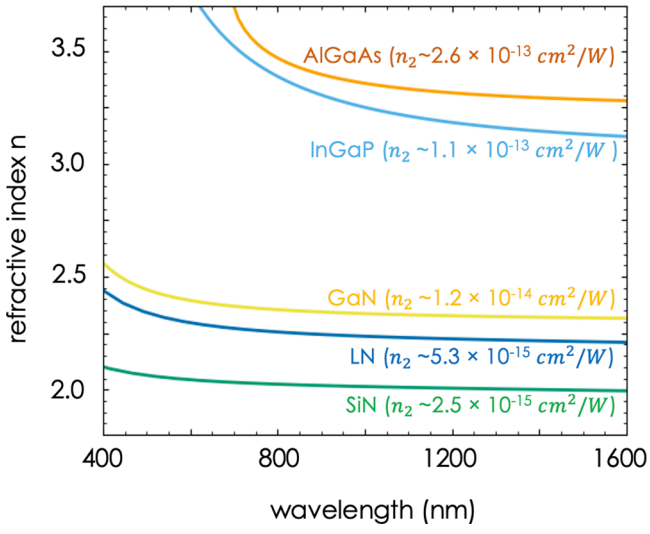

Figure 2. Refractive index of AlGaAs, InGaP, GaN, LN and SiN. As shown here, AlGaAs and InGaP have large slope near the visible spectrum, while GaN, LN, and SiN have an approximately linear slope across the wavelengths studied.

https://doi.org/10.1021/acsphotonics.4c01238
ACS Photonics 2025, 12, 118−127

have a flat and nearly linear dispersion in the relevant wavelength range, which simplifies achieving phase matching. As a result, assuming a signal wavelength of 1550 nm, the minimum idler wavelength for GaN, LN and SiN, is 700 nm, 600 nm, and 500 nm, respectively.

Achieving phase matching becomes challenging when the idler photon wavelength approaches the electronic band gap of the material. For materials like $Al_{0.3}Ga_{0.7}As$ and $In_{0.48}Ga_{0.52}P$ (denoted simply as AlGaAs and InGaP below), with band-edge transitions near 700 nm and 650 nm, respectively, the nonlinear increase in the refractive index hinders broadband phase matching for visible-wavelength idler photons as shown in Figure 2; however, because AlGaAs and InGaP are both cubic crystals with $F\bar{4}3m$ symmetry,[43,44] their $\chi^{(3)}_{ijkl}$ tensors have nonvanishing elements for $[k = l, i = j]$ and $[i = k, j = l]$, where the subscripts i, j, k, and l denote the signal, idler, and two pump fields for the SFWM process, respectively. Consequently, instead of restricting the pump, signal, and idler photons to all have the same polarization, which we denote as Type-0 pair generation (following the conventions for SPDC[40]), a cross-polarized pump-pair polarization scheme can also be utilized, which we denote as Type-1. As shown in Table 1, for Type-1 pair generation, the nonzero element $\chi^{(3)}_{xxyy}$ allows for pumping the TM mode to generate signal-idler pairs in the TE mode. The $\chi^{(3)}_{xxyy}$ values used for Type-1 generation are taken to be half of $\chi^{(3)}_{xxxx}$ as an approximation.[45] This cross-polarized scheme can be leveraged to achieve phase-matching for large signal-idler wavelength separation since the effective indices of the TM pump and TE pairs can be independently engineered through the waveguide geometry. In the numerical simulations in the following section, we explore pair generation for both Type-0 (for GaN, SiN, and LN) and Type-1 (for AlGaAs and InGaP) schemes.

Table 1. Relevant Polarization Schemes for Type-0 (Copolarized Pump and Pairs) and Type-1 (Crosspolarized Pump and Pairs) Pair Generation via SFWM That Are Permitted by the Nonvanishing Tensor Values of $\chi^{(3)}$

	Pump & Pump	Signal & Idler	AlGaAs	InGaP
Type 0	TE + TE	TE + TE	$\chi^{(3)}_{xxxx}$	$\chi^{(3)}_{xxxx}$
Type 1	TM + TM	TE + TE	$\chi^{(3)}_{xyxy}\chi^{(3)}_{xxyy}$	$\chi^{(3)}_{xyxy}\chi^{(3)}_{xxyy}$

Simulations. In the previous section, the design of broadband photon pair sources using SFWM in nonlinear materials was introduced, with a focus on achieving phase matching between the pump, signal, and idler modes. Here, we utilize the Ansys Lumerical finite difference eigenmode solver to tailor waveguide geometries for phase matching at specified wavelengths. We aim for the signal photon to be within the telecom C-band at 1550 nm to minimize optical fiber propagation loss for long-distance transmission. In our approach, depicted in Figure 1, we sweep the idler wavelength starting from 1550 nm to determine the point where geometry modifications cannot achieve the zero frequency mismatch condition. The pump angular frequency, determined by $\omega_p = (\omega_i + \omega_s)/2$, varies as the idler wavelength is swept and the signal wavelength remains fixed at 1550 nm.

As a specific case study, we model phase matching in these materials with an idler photon at 775 nm and a signal photon at 1550 nm, setting the pump wavelength at 1033.3 nm for energy conservation. The resulting frequency mismatch, $\Delta w = \frac{w_i n_s + w_s n_i}{2n_p} - w_p$, is analyzed for various waveguide geometries shown in Figure 3. In this model, we employ Type-0 phase matching for SiN, LN, and GaN, leveraging their relatively flat refractive index curves. For AlGaAs and InGaP,

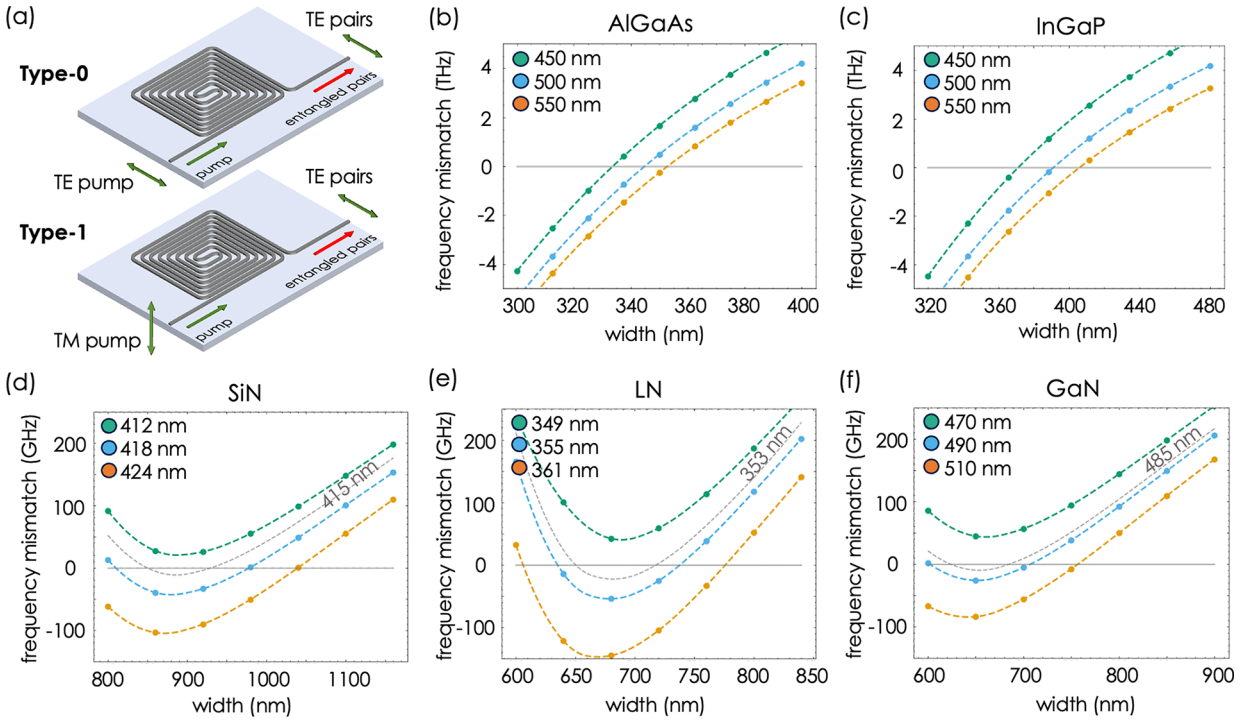

Figure 3. Frequency mismatch simulations for different waveguide dimensions assuming linear waveguides. Type-0 phase-matching is used for SiN, GaN and LN, while Type-1 is used for AlGaAs and InGaP.

https://doi.org/10.1021/acsphotonics.4c01238
ACS Photonics 2025, 12, 118−127

which exhibit significant refractive index variation across the selected wavelengths, we use Type-1 phase matching. In our simulations for AlGaAs and InGaP, we set the waveguide dimensions near 350 nm x 500 nm, favoring TM mode confinement for the pump mode. Due to the reduced confinement of the TE mode using this structure at visible and telecom wavelengths, the mode extends into the SiO_2 cladding, thus lowering the effective index at these wavelengths. Note that for SiN and LN, the waveguides have only bottom SiO_2 cladding with a top air-cladding to increase mode confinement in the waveguide, because these materials have relatively low refractive index contrast. Since the nonlinear interaction only occurs within the waveguide, weak mode confinement would be detrimental to the performance of these low-index contrast platforms. For the other material systems that have considerably larger refractive index contrast, the SiO_2 cladding surrounds the entire waveguide. For ring resonators, the simulation procedure is similar to a straight waveguide; however, when building the structure, an additional parameter, bend radius, is included in addition to width and height of the waveguide. The simulation is modified to solve Maxwell's equations in a cylindrical coordinate system for a given bend radius (compared to a Cartesian coordinate system for the straight waveguide). Here, the propagation constant becomes an angular propagation constant and the effective index becomes dependent on the bend.

RESULTS AND DISCUSSION

Simulations for SiN, LN, and GaN suggest that zero frequency mismatch can be achieved through Type-0 generation, provided that waveguide dimensions are optimized. For those materials, their phase matching trends consists of two regimes. In the first regime, the trend is flat, and the change in frequency mismatch remains small within a certain waveguide width. In the second regime, as the waveguide width is further increased or decreased, the frequency mismatch increases linearly with the width. Interestingly, this behavior indicates that for SiN, GaN, and LN, an optimum thickness exists within a small window that permits ≤10 GHz frequency mismatch for 100 nm variation in waveguide width. Because fabrication errors more severely affect the waveguide width, the first regime is an optimal design point for minimizing the impact of these errors. For SiN, this specific height is 415 nm, and the frequency mismatch is within ±10 GHz with widths ranging from 840 nm to 950 nm. Similar results are found for LN and GaN, which are shown in Table 2.

To demonstrate the fabrication tolerance and application in choosing the optimum waveguide structure, we use GaN as an example as shown in Figure 4. We show the frequency mismatch with a wider range of waveguide thicknesses in Figure 4(a), and the vector field of phase-matching sensitivity with respect to fabrication deviation from the target design is shown in Figure 4(b). The vector field is a representation of $\frac{\partial \text{Mismatch(width, height)}}{\partial \text{width}}$ and $\frac{\partial \text{Mismatch(width, height)}}{\partial \text{height}}$. This serves as a direct indication of the fabrication tolerance. In areas where the magnitude of the vector is small, the phase-matching condition is less affected by changes in the waveguide width and height. A range of different dimensions can successfully achieve zero mismatch, shown by the solid black line in Figure 4(b), but the gradient plays an important role in deciding the optimum dimension that maximizes the yield. In contrast, Figure 3(b,c) shows that AlGaAs and InGaP are more sensitive to waveguide dimensions, displaying a narrower range of suitable widths to achieve optimal phase matching. This sensitivity is a consequence of the Type-1 phase-matching scheme used for these materials to extend the signal-idler wavelength separation, which suggests tighter tolerances for the waveguide height and width in fabrication.

Table 2. Waveguide Cross-section Values for Each Material Platform to Achieve Optimal Pair Generation with Minimal Frequency Mismatch and Fabrication Process Variation Tolerance in the Waveguide Widths for Fixed Waveguide Heights

	Height (nm)	Width (nm)	Frequency Mismatch (GHz)
SiN	415	840−950	≤10
LN	353	640−740	≤20
GaN	485	610−700	≤10

From the optimized designs with zero frequency mismatch predicted by Figure 3, we next calculated the SFWM pair generation rate (PGR), which is shown as a function of wavelength and waveguide length (assuming a linear waveguide is used to generate entangled-photon pairs) in Figure 5. Figure 5(a) shows the pair generation rate heatmap for GaN and employs the following equation to determine the PGR in the low power limit for straight waveguides:[41,46,47]

$$\text{PGR}_{\text{straight}} \approx \gamma^2 P^2 L_{\text{eff}}^2 \text{sinc}^2(\Delta k L/2) \tag{4}$$

where γ is the nonlinear parameter defined as $\frac{n_2}{\lambda A_{\text{eff}}}$, P is the optical pump power, and $L_{\text{eff}} = \frac{1-e^{-\alpha L}}{\alpha}$. A_{eff} is the effective area that takes into account the mode overlap of the signal, idler, and pump fields[48] (see Supporting Information), Δk is the wavevector mismatch, α is the scattering loss and $n_2 = \frac{3\chi^{(3)}}{4n^2\epsilon_0 c}$ is the Kerr coefficient. Here, it is assumed that the pump is in the lower power regime.

The process for generating the plot is as follows: First, the waveguide dimensions required to achieve zero frequency mismatch are determined (Figure 5). As previously mentioned, this cross section results in the minimized mode area for zero frequency mismatch as well as high tolerance to process variations in fabrication. Using these dimensions, the effective index of the target modes are simulated over a wavelength range from 700 to 1600 nm. Then Δk is calculated as a function of wavelength and substituted into eq 4 to yield the pair generation rate for a straight waveguide as a function of wavelength. Note that the pump wavelength is fixed at 1033.3 nm, while we sweep the signal and idler wavelengths from 700 to 1600 nm and numerically calculate the pair generation rate across all wavelength combinations. The wavelength of the pump, signal, and idler photon thus must satisfy $\frac{1}{\lambda_s} + \frac{1}{\lambda_i} = \frac{2}{\lambda_p}$.

The heatmaps for SiN and LN look very similar to that of GaN but the magnitude of their PGR is different. The maximum PGR values for those materials are marked on the scale bar of GaN for comparison. For the maximum pair generation rate comparison given minimal wavevector mismatch, we set the scattering loss to 0.1 dB/cm, waveguide length, L, to be 8 mm for GaN, LN and SiN, and 0.8 mm for AlGaAs and InGaP. Figure 5(b) shows the PGR heatmap for AlGaAs, with the maximum PGR rate of InGaP marked for comparison. A key difference between the PGR behavior for

https://doi.org/10.1021/acsphotonics.4c01238
ACS Photonics 2025, 12, 118−127

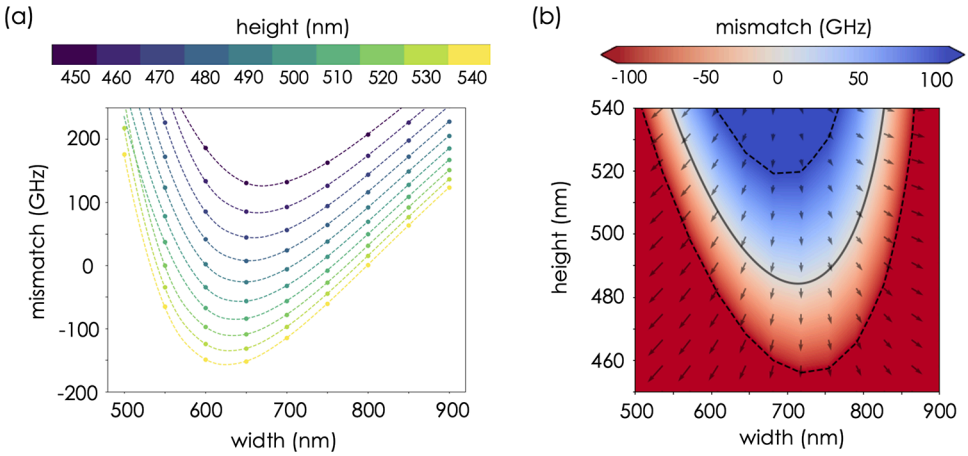

Figure 4. A complete phase matching profile for GaN is shown in (a) with a broader range of height and width. (b) Heatmap as a combination of vector field and mismatch. The dashed contour lines show when the mismatch value is at ±100 GHz. The solid black line indicates dimensions for zero frequency mismatch.

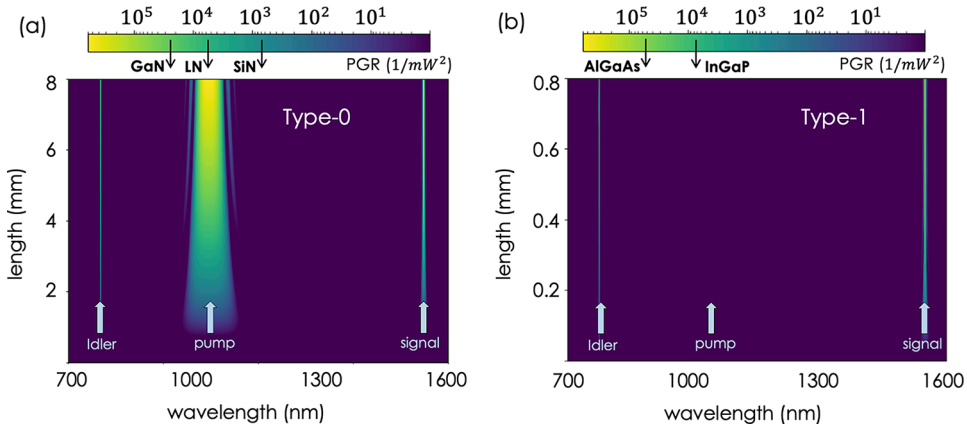

Figure 5. Pair generation rate (PGR) heatmaps for Type-0 (a) and Type-1 (b) phase-matching as a function of wavelength and waveguide propagation length. The relative PGRs for Type-0 (GaN, LN, and SiN) and Type-1 (AlGaAs and InGaP) are shown on the color bar. For Type-0, both visible-telecom pair generation as well as pair generation in a narrow spectral region adjacent to the pump are possible, whereas Type-1 only allows for visible-telecom generation due to the cross-polarized pump and signal/idler modes.

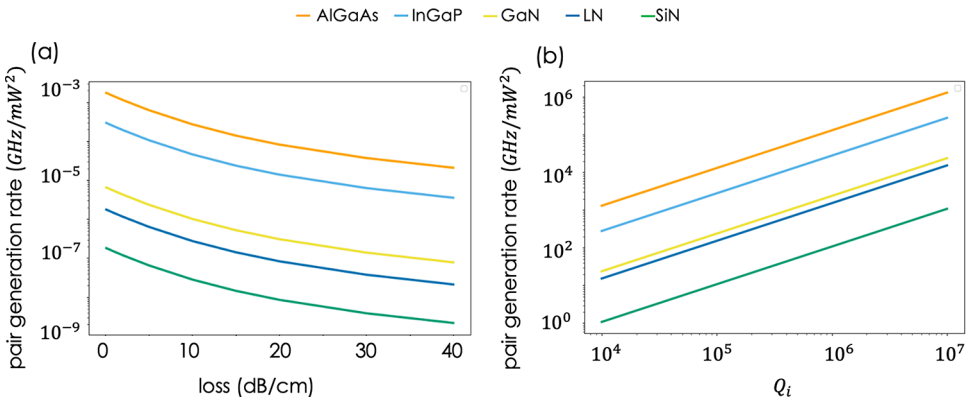

Figure 6. Comparison of pair generation rate for straight waveguide (a) and ring resonators (b). For ring resonators in (b), we set $Q_p = Q_s = 10^6$ and we sweep Q_i.

GaN, LN, and SiN in Figure 5(a) and the behavior for AlGaAs and InGaP in Figure 5(b) is the SFWM signal directly adjacent to the pump wavelength. For materials such as GaN, LN, and SiN, the effective refractive index (n_{eff}) remains relatively constant across the entire bandwidth. When generating entangled photon pairs near a pump wavelength of 1033 nm via SFWM, the refractive indices for signal (n_s), idler (n_i), and pump (n_p) photons are nearly identical, leading to minimal wavevector mismatch and maximal PGR as calculated through eq 4, resulting in pair generation near the pump in addition to the broadband pairs at 775 and 1550 nm. In contrast, for AlGaAs and InGaP, which utilize Type-1 generation, the

https://doi.org/10.1021/acsphotonics.4c01238
ACS Photonics 2025, 12, 118−127

refractive indices for signal and idler photons differ markedly from the pump photon, primarily because n_s and n_i stem from the fundamental TE mode, while n_p is derived from the TM mode, resulting in a larger wavevector mismatch.

Furthermore, the bandwidth near the signal and idler modes for AlGaAs and InGaP becomes progressively narrower as the waveguide length increases. This narrowing is a result of the accumulation of phase mismatch when the wavevector mismatch is nonzero. For short waveguides, the accumulated phase is small, but as the length increases, this nonzero wavevector mismatch causes the modes to become out of phase, limiting the wavelength range over which entangled photon pairs can be efficiently generated. One conclusion from this is that AlGaAs maintains a competitive PGR compared to GaN; however, the trade-off is fabrication tolerance: achieving the target cross section to achieve high PGR is more challenging in AlGaAs and InGaP, as precise control over waveguide dimensions within a few nanometers is crucial for optimizing performance.

The comparison of PGR values of different platforms in both straight waveguides and ring resonators is plotted in Figure 6. For Figure 6(a), we assume zero frequency mismatch and set the length of the waveguide to 10 mm. In the case of SiN, the experimentally attainable loss for this optimized cross section is as low as 1 dB/cm,[49] which corresponds to 10^{-7} GHz/mW^2 for a straight waveguide. Conversely, for AlGaAs and InGaP, although these materials experience higher loss > 1 dB/cm for these geometries, their PGRs are still significantly greater than that of SiN primarily due to the higher nonlinearity and larger refractive indices.

For ring resonators, the PGR is calculated using the following expression[50,51] (see Supporting Information):

$$\mathrm{PGR}_{\mathrm{ring}} = (\gamma P_{\mathrm{pump}})^2 \frac{8 v_s v_i {v_p}^2}{\pi^2 \omega_s \omega_i \omega_p} \frac{Q_s Q_i Q_p}{R^2} \tag{5}$$

where v_s, v_i, and v_p are the group velocity of signal, idler, and pump. Q_s, Q_i, and Q_p are the quality factor of signal, idler, and pump, respectively. R is the ring radius which we set to 40 μm in the numerical simulations in Figure 6(b). In this figure, we set Q_p and Q_s both to one million, which is a representative attainable value for each of the materials for the pump and signal wavelengths in this study, and we sweep Q_i.

While the majority of experimental studies on chip-scale entangled pair sources have focused on development in the telecom band, Lu et al. have reported visible-telecom pair generation via SFWM using a SiN microresonator.[14] In that work, a SiN microresonator with Q's of 1.52×10^5, 1.04×10^6, and 1.93×10^5 for wavelengths of 668 nm (idler), 933 nm (pump), and 1548 nm (signal), respectively, produced pairs at an on-chip rate of 10 MHz/mW^2. This rate is 1−2 orders of magnitude smaller than the sub-1 GHz/mW^2 from our modeling, most likely due to a combination of suboptimal phase matching and competing processes such as optical parametric oscillation at the pump wavelength that reduces the conversion efficiency.[14] For InGaP, Q's up to 4×10^5 (2×10^5) have been demonstrated at 1550 nm (775 nm),[36,39] which would correspond to rates exceeding 100 GHz/mW^2. For AlGaAs, > 30 GHz/mW^2 has been recently demonstrated in microring resonators with $Q > 10^6$ for C-band sources.[27,52] For GaN, Q's around 4×10^5 have been reported at 1550 nm,[38] while Q's approaching 30×10^6 have been reported in thin film LN.[53] These values provide some context for the potential performance for visible-telecom pair generation, which may guide future experiments with these materials that have yet to be explored.

Although AlGaAs and InGaP demonstrate a distinct advantage in terms of PGR over other materials in both straight waveguides and ring resonators, these figures are predicated on the achievement of perfect phase matching. However, in practice, achieving such precision is challenging due to limitations in fabrication accuracy. Even slight dimensional variations in AlGaAs and InGaP can cause deviations from an ideal phase mismatch. To compensate for these imperfections, thermal tuning may be employed to adjust and improve phase matching after the fabrication process. Additionally, wafer-scale fabrication allows for sweeping parameters to ensure full coverage of the zero frequency mismatch parameter space for a given waveguide thickness.[39] Conversely, materials such as GaN and LN are not as sensitive to such process variations. They not only achieve relatively high PGRs but also meet the phase matching conditions more readily, which makes them particularly attractive for practical applications where fabrication precision may not be as stringent. Additionally, they will likely exhibit lower propagation loss at 775 nm and ultimately exhibit broader bandwidth for higher PGRs deeper in the visible regime.

CONCLUSION

In this study, we compared different photonic material platforms for generating entangled photon pairs via spontaneous four-wave mixing to bridge the gap between long-distance communication at telecom wavelengths and visible-wavelength quantum sensors, processors, and memories. Through detailed numerical simulations, we found that materials such as AlGaAs and InGaP can achieve the highest pair generation rates for a given resonator quality factor Q, but they also have the most stringent requirements on the fabrication precision required to achieve optimal phase matching. Through a Type-1 cross-polarized phase-matching scheme, their idler wavelength can also be extended deeper into the visible regime. Other materials such as silicon nitride have a lower pair generation rate, but they can also benefit from industrial-standardized foundry manufacturing processes and exhibit a higher tolerance to fabrication process variations due to flat dispersion. Of all the materials studied, GaN may represent the optimal choice in that it exhibits a moderately large $\chi^{(3)}$ nonlinearity, less sensitivity to material parameters and process variations, and thus phase matching is relatively straightforward; however, low-loss GaN fabrication and processing, including various alloys such as AlGaN, AlN, and ScAlN, is an emerging direction for exciting future studies for nonlinear photonics and broadband pair generation.[54,55]

Another important consideration is the line width of the signal and idler photons. For applications in quantum networking and distributed computing, the idler photons may interact with a variety of quantum systems with optical transitions in the visible regime such as those indicated in Figure 1. This interaction may be done through resonant linear transmission or reflection from the quantum systems or through two-photon interference, such as Bell-state measurements for entanglement swapping and teleportation. In these cases, not only is the resonance wavelength of the idler photon important, but for high-fidelity and high-efficiency entanglement swapping, the spatial, spectral, and temporal modes of the idler photon and the photon emitted from the quantum

https://doi.org/10.1021/acsphotonics.4c01238
ACS Photonics 2025, 12, 118−127

system must also match. For example, the zero-phonon line widths of color centers in diamond and silicon carbide[56] can be as low as ∼10 MHz. Generating an idler photon with a similar line width would require Q on the order of 40×10^6, which is attainable with SiN. On the other hand, hBN quantum defects with spin-photon transitions and semiconductor QDs have zero-phonon line widths ranging from ∼100−500 MHz. These line widths correspond to Q's on the order of 10^5−10^6, which is attainable with each of the studied material platforms.[15,57]

■ ASSOCIATED CONTENT

Data Availability Statement

All data that supports the findings of this study are available upon request.

Supporting Information

The Supporting Information is available free of charge at https://pubs.acs.org/doi/10.1021/acsphotonics.4c01238.

The document describes our model simulating nonlinear phase matching contributions, calculations of the modal effective areas, and the generalized pair generation rate formula used in the main text (PDF)

■ AUTHOR INFORMATION

Corresponding Author

Galan Moody − *Electrical and Computer Engineering Department, University of California, Santa Barbara, California 93106, United States;* orcid.org/0000-0002-6265-2034; Email: moody@ucsb.edu

Authors

Liao Duan − *Department of Physics, University of California, Santa Barbara, California 93106, United States*

Trevor J. Steiner − *Materials Department, University of California, Santa Barbara, California 93106, United States*

Paolo Pintus − *Electrical and Computer Engineering Department, University of California, Santa Barbara, California 93106, United States; Physics Department, University of Cagliari, Monserrato 09042, Italy*

Lillian Thiel − *Electrical and Computer Engineering Department, University of California, Santa Barbara, California 93106, United States*

Joshua E. Castro − *Electrical and Computer Engineering Department, University of California, Santa Barbara, California 93106, United States*

John E. Bowers − *Electrical and Computer Engineering Department, University of California, Santa Barbara, California 93106, United States; Materials Department, University of California, Santa Barbara, California 93106, United States*

Complete contact information is available at: https://pubs.acs.org/10.1021/acsphotonics.4c01238

Funding

This work was supported by the NSF Quantum Foundry through the Q-AMASE-i Program (Grant No. DMR-1906325), the NSF CAREER Program (Grant No. 2045246), the Keysight University Research Program, and the Eddleman Center for Quantum Innovation. L. T. acknowledges support from the NSF Graduate Research Fellowship Program.

Notes

The authors declare no competing financial interest.

■ REFERENCES

(1) Awschalom, D.; Berggren, K. K.; Bernien, H.; Bhave, S.; Carr, L. D.; Davids, P.; Economou, S. E.; Englund, D.; Faraon, A.; Fejer, M.; Guha, S.; Gustafsson, M. V.; Hu, E.; Jiang, L.; Kim, J.; Korzh, B.; Kumar, P.; Kwiat, P. G.; Loncar, M.; Lukin, M. D.; Miller, D. A.B.; Monroe, C.; Nam, S. W.; Narang, P.; Orcutt, J. S.; Raymer, M. G.; Safavi-Naeini, A. H.; Spiropulu, M.; Srinivasan, K.; Sun, S.; Vuckovic, J.; Waks, E.; Walsworth, R.; Weiner, A. M.; Zhang, Z. Development of quantum interconnects (quics) for next-generation information technologies. *PRX Quantum* **2021**, *2*, 017002.

(2) Moody, G.; Sorger, V. J; Blumenthal, D. J; Juodawlkis, P. W; Loh, W.; Sorace-Agaskar, C.; Jones, A. E; Balram, K. C; Matthews, J. C F; Laing, A.; Davanco, M.; Chang, L.; Bowers, J. E; Quack, N.; Galland, C.; Aharonovich, I.; Wolff, M. A; Schuck, C.; Sinclair, N.; Loncar, M.; Komljenovic, T.; Weld, D.; Mookherjea, S.; Buckley, S.; Radulaski, M.; Reitzenstein, S.; Pingault, B.; Machielse, B.; Mukhopadhyay, D.; Akimov, A.; Zheltikov, A.; Agarwal, G. S; Srinivasan, K.; Lu, J.; Tang, H. X; Jiang, W.; McKenna, T. P; Safavi-Naeini, A. H; Steinhauer, S.; Elshaari, A. W; Zwiller, V.; Davids, P. S; Martinez, N.; Gehl, M.; Chiaverini, J.; Mehta, K. K; Romero, J.; Lingaraju, N. B; Weiner, A. M; Peace, D.; Cernansky, R.; Lobino, M.; Diamanti, E.; Vidarte, L. T.; Camacho, R. M Roadmap on integrated quantum photonics. *Journal of Physics: Photonics* **2022**, *4*, 012501.

(3) Sukachev, D. D.; Sipahigil, A.; Nguyen, C. T.; Bhaskar, M. K.; Evans, R. E.; Jelezko, F.; Lukin, M. D. Silicon-vacancy spin qubit in diamond: a quantum memory exceeding 10 ms with single-shot state readout. *Physical review letters* **2017**, *119*, 223602.

(4) Wang, P.; Luan, C.-Y.; Qiao, M.; Um, M.; Zhang, J.; Wang, Y.; Yuan, X.; Gu, M.; Zhang, J.; Kim, K. Single ion qubit with estimated coherence time exceeding one hour. *Nat. Commun.* **2021**, *12*, 233.

(5) Pino, J. M.; Dreiling, J. M.; Figgatt, C.; Gaebler, J. P.; Moses, S. A.; Allman, M. S.; Baldwin, C. H.; Foss-Feig, M.; Hayes, D.; Mayer, K.; Ryan-Anderson, C.; Neyenhuis, B. Demonstration of the trapped-ion quantum CCD computer architecture. *Nature* **2021**, *592*, 209−213.

(6) Norcia, M. A.; Cairncross, W. B.; Barnes, K.; Battaglino, P.; Brown, A.; Brown, M. O.; Cassella, K.; Chen, C.-A.; Coxe, R.; Crow, D.; Epstein, J.; Griger, C.; Jones, A. M. W.; Kim, H.; Kindem, J. M.; King, J.; Kondov, S. S.; Kotru, K.; Lauigan, J.; Li, M.; Lu, M.; Megidish, E.; Marjanovic, J.; McDonald, M.; Mittiga, T.; Muniz, J. A.; Narayanaswami, S.; Nishiguchi, C.; Notermans, R.; Paule, T.; Pawlak, K. A.; Peng, L. S.; Ryou, A.; Smull, A.; Stack, D.; Stone, M.; Sucich, A.; Urbanek, M.; van de Veerdonk, R. J. M.; Vendeiro, Z.; Wilkason, T.; Wu, T.-Y.; Xie, X.; Zhang, X.; Bloom, B. J. Midcircuit Qubit Measurement and Rearrangement in a Yb 171 Atomic Array. *Physical Review X* **2023**, *13*, 041034.

(7) Buser, G.; Mottola, R.; Cotting, B.; Wolters, J.; Treutlein, P. Single-photon storage in a ground-state vapor cell quantum memory. *PRX quantum* **2022**, *3*, 020349.

(8) Maring, N.; Fyrillas, A.; Pont, M.; Ivanov, E.; Stepanov, P.; Margaria, N.; Hease, W.; Pishchagin, A.; Lemaitre, A.; Sagnes, I.; Au, T. H.; Boissier, S.; Bertasi, E.; Baert, A.; Valdivia, M.; Billard, M.; Acar, O.; Brieussel, A.; Mezher, R.; Wein, S. C.; Salavrakos, A.; Sinnott, P.; Fioretto, D. A.; Emeriau, P.-E.; Belabas, N.; Mansfield, S.; Senellart, P.; Senellart, J.; Somaschi, N. A versatile single-photon-based quantum computing platform. *Nat. Photonics* **2024**, *18*, 603−609.

(9) Borregaard, J.; Pichler, H.; Schröder, T.; Lukin, M. D.; Lodahl, P.; Sørensen, A. S. One-way quantum repeater based on near-deterministic photon-emitter interfaces. *Physical Review X* **2020**, *10*, 021071.

(10) Singh, A.; Li, Q.; Liu, S.; Yu, Y.; Lu, X.; Schneider, C.; Hofling, S.; Lawall, J.; Verma, V.; Mirin, R.; Nam, S. W.; Liu, J.; Srinivasan, K. Quantum frequency conversion of a quantum dot single-photon source on a nanophotonic chip. *Optica* **2019**, *6*, 563−569.

(11) Zaske, S.; Lenhard, A.; Keßler, C. A.; Kettler, J.; Hepp, C.; Arend, C.; Albrecht, R.; Schulz, W.-M.; Jetter, M.; Michler, P.; Becher, C. others Visible-to-telecom quantum frequency conversion of light

from a single quantum emitter. *Physical review letters* **2012**, *109*, 147404.
(12) Bock, M.; Eich, P.; Kucera, S.; Kreis, M.; Lenhard, A.; Becher, C.; Eschner, J. High-fidelity entanglement between a trapped ion and a telecom photon via quantum frequency conversion. *Nat. Commun.* **2018**, *9*, 1998.
(13) Morrison, C. L.; Rambach, M.; Koong, Z. X.; Graffitti, F.; Thorburn, F.; Kar, A. K.; Ma, Y.; Park, S.-I.; Song, J. D.; Stoltz, N. G.; Bouwmeester, D.; Fedrizzi, A.; Gerardot, B. D. A bright source of telecom single photons based on quantum frequency conversion. *Appl. Phys. Lett.* **2021**, DOI: 10.1063/5.0045413.
(14) Lu, X.; Li, Q.; Westly, D. A.; Moille, G.; Singh, A.; Anant, V.; Srinivasan, K. Chip-integrated visible−telecom entangled photon pair source for quantum communication. *Nat. Phys.* **2019**, *15*, 373−381.
(15) Moody, G.; Chang, L.; Steiner, T. J.; Bowers, J. E. Chip-scale nonlinear photonics for quantum light generation. *AVS Quantum Science* **2020**, *2*, 041702.
(16) Pelucchi, E.; Fagas, G.; Aharonovich, I.; Englund, D.; Figueroa, E.; Gong, Q.; Hannes, H.; Liu, J.; Lu, C.-Y.; Matsuda, N.; Pan, J.-W.; Schreck, F.; Sciarrino, F.; Silberhorn, C.; Wang, J.; Jons, K. D. The potential and global outlook of integrated photonics for quantum technologies. *Nature Reviews Physics* **2022**, *4*, 194−208.
(17) Olislager, L.; Cussey, J.; Nguyen, A. T.; Emplit, P.; Massar, S.; Merolla, J.-M.; Huy, K. P. Frequency-bin entangled photons. Physical Review A—Atomic. *Molecular, and Optical Physics* **2010**, *82*, 013804.
(18) Caspani, L.; Xiong, C.; Eggleton, B. J.; Bajoni, D.; Liscidini, M.; Galli, M.; Morandotti, R.; Moss, D. J. Integrated sources of photon quantum states based on nonlinear optics. *Light: Science & Applications* **2017**, *6*, e17100−e17100.
(19) James, D. F. V.; Kwiat, P. G.; Munro, W. J.; White, A. G. Measurement of qubits. *Phys. Rev. A* **2001**, *64*, 052312.
(20) Feng, L.-T.; Zhang, M.; Xiong, X.; Chen, Y.; Wu, H.; Li, M.; Guo, G.-P.; Guo, G.-C.; Dai, D.-X.; Ren, X.-F. On-chip transverse-mode entangled photon pair source. *npj Quantum Information* **2019**, DOI: 10.1038/s41534-018-0121-z.
(21) Yin, J.; Li, Y.-H.; Liao, S.-K.; Yang, M.; Cao, Y.; Zhang, L.; Ren, J.-G.; Cai, W.-Q.; Liu, W.-Y.; Li, S.-L.; Shu, R.; Huang, Y.-M.; Deng, L.; Li, L.; Zhang, Q.; Liu, N.-L.; Chen, Y.-A.; Lu, C.-Y.; Wang, X.-B.; Xu, F.; Wang, J.-Y.; Peng, C.-Z.; Ekert, A. K.; Pan, J.-W. Entanglement-based secure quantum cryptography over 1,120 kilometres. *Nature* **2020**, *582*, 501−505.
(22) Yin, J.; Cao, Y.; Li, Y.-H.; Ren, J.-G.; Liao, S.-K.; Zhang, L.; Cai, W.-Q.; Liu, W.-Y.; Li, B.; Dai, H.; Li, M.; Huang, Y.-M.; Deng, L.; Li, L.; Zhang, Q.; Liu, N.-L.; Chen, Y.-A.; Lu, C.-Y.; Shu, R.; Peng, C.-Z.; Wang, J.-Y.; Pan, J.-W. Satellite-to-ground entanglement-based quantum key distribution. *Physical review letters* **2017**, *119*, 200501.
(23) Boitier, F.; Orieux, A.; Autebert, C.; Lemaître, A.; Galopin, E.; Manquest, C.; Sirtori, C.; Favero, I.; Leo, G.; Ducci, S. Electrically injected photon-pair source at room temperature. *Physical review letters* **2014**, *112*, 183901.
(24) Orieux, A.; Eckstein, A.; Lemaitre, A.; Filloux, P.; Favero, I.; Leo, G.; Coudreau, T.; Keller, A.; Milman, P.; Ducci, S. Direct Bell states generation on a III-V semiconductor chip at room temperature. *Physical review letters* **2013**, *110*, 160502.
(25) Zhao, J.; Ma, C.; Rüsing, M.; Mookherjea, S. High quality entangled photon pair generation in periodically poled thin-film lithium niobate waveguides. *Physical review letters* **2020**, *124*, 163603.
(26) Baboux, F.; Moody, G.; Ducci, S. Nonlinear integrated quantum photonics with AlGaAs. *Optica* **2023**, *10*, 917.
(27) Steiner, T. J.; Shen, M.; Castro, J. E.; Bowers, J. E.; Moody, G. Continuous entanglement distribution from an AlGaAs-on-insulator microcomb for quantum communications. *Optica Quantum* **2023**, *1*, 55−62.
(28) Alexander, K.; Bahgat, A.; Benyamini, A.; Black, D.; Bonneau, D.; Burgos, S.; Burridge, B.; Campbell, G.; Catalano, G.; Ceballos, A. A manufacturable platform for photonic quantum computing. *arXiv*, 2024. https://arxiv.org/abs/2404.17570 (accessed October 17, 2024).
(29) Franson, J. D. Bell inequality for position and time. *Phys. Rev. Lett.* **1989**, *62*, 2205−2208.
(30) Terhal, B. M.; Horodecki, P. Schmidt number for density matrices. *Phys. Rev. A* **2000**, *61*, 040301.
(31) Lu, H.-H.; Liscidini, M.; Gaeta, A. L.; Weiner, A. M.; Lukens, J. M. Frequency-bin photonic quantum information. *Optica* **2023**, *10*, 1655−1671.
(32) Dutt, A.; Mohanty, A.; Gaeta, A. L.; Lipson, M. Nonlinear and quantum photonics using integrated optical materials. *Nat. Rev. Mater.* **2024**, *9*, 321−346.
(33) Söller, C.; Brecht, B.; Mosley, P. J.; Zang, L. Y.; Podlipensky, A.; Joly, N. Y.; Russell, P. S. J.; Silberhorn, C. Bridging visible and telecom wavelengths with a single-mode broadband photon pair source. *Phys. Rev. A* **2010**, *81*, 031801.
(34) Clausen, C.; Bussieres, F.; Tiranov, A.; Herrmann, H.; Silberhorn, C.; Sohler, W.; Afzelius, M.; Gisin, N. A source of polarization-entangled photon pairs interfacing quantum memories with telecom photons. *New J. Phys.* **2014**, *16*, 093058.
(35) Schunk, G.; Vogl, U.; Strekalov, D. V.; Förtsch, M.; Sedlmeir, F.; Schwefel, H. G.; Göbelt, M.; Christiansen, S.; Leuchs, G.; Marquardt, C. Interfacing transitions of different alkali atoms and telecom bands using one narrowband photon pair source. *Optica* **2015**, *2*, 773−778.
(36) Akin, J.; Zhao, Y.; Misra, Y.; Haque, A.; Fang, K. InGaP chi(2) integrated photonics platform for broadband, ultra-efficient nonlinear conversion and entangled photon generation. *arXiv* **2024**, DOI: 10.48550/arXiv.2406.02434.
(37) Kues, M.; Reimer, C.; Lukens, J. M.; Munro, W. J.; Weiner, A. M.; Moss, D. J.; Morandotti, R. Quantum optical microcombs. *Nat. Photonics* **2019**, *13*, 170−179.
(38) Zeng, H.; He, Z.-Q.; Fan, Y.-R.; Luo, Y.; Lyu, C.; Wu, J.-P.; Li, Y.-B.; Liu, S.; Wang, D.; Zhang, D.-C.; Zeng, J.-J.; Deng, G.-W.; Wang, Y.; Song, H.-Z.; Wang, Z.; You, L.-X.; Guo, K.; Sun, C.-Z.; Luo, Y.; Guo, G.-C.; Zhou, Q. Quantum Light Generation Based on GaN Microring toward Fully On-Chip Source. *Phys. Rev. Lett.* **2024**, *132*, 133603.
(39) Thiel, L.; Castro, J. E.; Steiner, T. J.; Nguyen, C.; Pechilis, A.; Duan, L.; Lewis, N.; Cole, G. D.; Bowers, J. E.; Moody, G. Wafer-scale fabrication of InGaP-on-insulator for nonlinear and quantum photonic applications. *Appl. Phys. Lett.* **2024**, *125*, 131102.
(40) Boyd, R. W.; Gaeta, A. L.; Giese, E. *Springer Handbook of Atomic, Molecular, and Optical Physics*; Springer, 2008; pp 1097−1110.
(41) Helt, L. G.; Liscidini, M.; Sipe, J. E. How does it scale? Comparing quantum and classical nonlinear optical processes in integrated devices. *JOSA B* **2012**, *29*, 2199−2212.
(42) Gupta, R.; Happer, W.; Lam, L.; Svanberg, S. Hyperfine-structure measurements of excited S states of the stable isotopes of potassium, rubidium, and cesium by cascade radio-frequency spectroscopy. *Phys. Rev. A* **1973**, *8*, 2792.
(43) Yariv, A.; Yeh, P. *Optical Waves in Crystal Propagation and Control of Laser radiation*; John Wiley and Sons, Inc., New York, NY, 1983.
(44) Sadao, A. GaAs, AlAs, and AlxGa1-xAs: Material parameters for use in research and device applications. *J. Appl. Phys.* **1985**, *58*, R1−R29.
(45) Hutchings, D. C.; Wherrett, B. S. Theory of the anisotropy of ultrafast nonlinear refraction in zinc-blende semiconductors. *PHYSICAL REVIEW B* **1995**, *52*, 8150−8159.
(46) Brainis, E. Four-photon scattering in birefringent fibers. *Phys. Rev. A* **2009**, *79*, 023840.
(47) Clemmen, S.; Huy, K. P.; Bogaerts, W.; Baets, R. G.; Emplit, P.; Massar, S. Continuous wave photon pair generation in silicon-on-insulator waveguides and ring resonators. *Opt. Express* **2009**, *17*, 16558−16570.
(48) Garay-Palmett, K.; Corona, M.; U'Ren, A. Spontaneous parametric processes in optical fibers: a comparison. *REVISTA MEXICANA DE FÍSICA* **2011**, *57*, 6−14.
(49) Buzaverov, K. A.; Baburin, A. S.; Sergeev, E. V.; Avdeev, S. S.; Lotkov, E. S.; Andronik, M.; Stukalova, V. E.; Baklykov, D. A.;

Dyakonov, I. V.; Skryabin, N. N.; Saygin, M. Y.; Kulik, S. P.; Ryzhikov, I. A.; Rodionov, I. A. Low-loss silicon nitride photonic ICs for near-infrared wavelength bandwidth. *Opt. Express* **2023**, *31*, 16227−16242.
(50) Helt, L. G.; Yang, Z.; Liscidini, M.; Sipe, J. E. Spontaneous four-wave mixing in microring resonators. *Optics letters* **2010**, *35*, 3006−3008.
(51) Azzini, S.; Grassani, D.; Strain, M. J.; Sorel, M.; Helt, L. G.; Sipe, J.; Liscidini, M.; Galli, M.; Bajoni, D. Ultra-low power generation of twin photons in a compact silicon ring resonator. *Opt. Express* **2012**, *20*, 23100−23107.
(52) Steiner, T. J.; Castro, J. E.; Chang, L.; Dang, Q.; Xie, W.; Norman, J.; Bowers, J. E.; Moody, G. Ultrabright Entangled-Photon-Pair Generation from an AlGaAs-On-Insulator Microring Resonator. *PRX Quantum* **2021**, *2*, 010337.
(53) Zhu, X.; Hu, Y.; Lu, S.; Warner, H. K.; Li, X.; Song, Y.; Magalhaes, L.; Shams-Ansari, A.; Cordaro, A.; Sinclair, N.; Loncar, M. others Twenty-nine million intrinsic Q-factor monolithic micro-resonators on thin-film lithium niobate. *Photonics Research* **2024**, *12*, A63−A68.
(54) Liu, X.; Bruch, A. W.; Tang, H. X. Aluminum nitride photonic integrated circuits: from piezo-optomechanics to nonlinear optics. *Advances in Optics and Photonics* **2023**, *15*, 236−317.
(55) Xu, T.; Liu, Y.; Pu, Y.; Yang, Y.; Zhong, Q.; Zhao, X.; Qiu, Y.; Dong, Y.; Wu, T.; Zheng, S. Silicon-integrated scandium-doped aluminum nitride electro-optic modulator. *arXiv*, 2024. https://arxiv.org/abs/2405.18717 (accessed October 17, 2024).
(56) Lukin, D. M.; Guidry, M. A.; Vučković, J. Integrated Quantum Photonics with Silicon Carbide: Challenges and Prospects. *PRX Quantum* **2020**, *1*, 020102.
(57) Azzam, S. I.; Parto, K.; Moody, G. Prospects and challenges of quantum emitters in 2D materials. *Appl. Phys. Lett.* **2021**, *118*, 240502.

https://doi.org/10.1021/acsphotonics.4c01238
ACS Photonics 2025, 12, 118−127